Article:

Jirankova, E and Lazecky, M orcid.org/0000-0001-8179-5949 (2022) Ground surface uplift during subsidence trough formation due to longwall mining in the shaft protection pillar of the CSM Mine. Bulletin of Engineering Geology and the Environment, 81 (9). 389. ISSN 1435-9529

https://doi.org/10.1007/s10064-022-02896-5

Ground surface uplift during subsidence trough formation due to longwall mining in the shaft protection pillar of the CSM Mine

Eva Jirankova[a,*], Milan Lazecky[b,c]

[a] Institute of Geonics of the Czech Academy of Sciences, Studentska 1768, 708 00 Ostrava-Poruba, Czech Republic,

[b] University of Leeds, Woodhouse Lane, Leeds, LS2 9JT, United Kingdom

[c] IT4Innovations, VSB-TU Ostrava, 17. Listopadu 15, 708 00 Ostrava-Poruba, Czech Republic

* Corresponding author's email: eva.jirankova@ugn.cas.cz

Abstract

Ground surface uplift was detected at the start of longwall mining, a significant part of which is situated in the shaft protection pillar Sever of the CSM Mine in the Czech Republic. The largest uplift was found to be 23 mm, by the levelling method of surface points with height connections to non-mined areas. Due to the length of the connection to the non-influenced area, precise levelling was chosen to observe the vertical displacements and prove the displacement values using a confidence interval with 5% risk. This article aims to clarify the cause of ground surface uplift during longwall mining. Therefore, the height changes of the given area were extracted also from satellite radar interferometry (InSAR). The changes of the observed ground surface were compared with the empirical subsidence. The largest difference between the measured and empirical surface subsidence was 85 mm and occurred in the period before the ground surface uplift. Spatiotemporal evaluation of the data was used to determine the presumed cause of the occurrence of surface uplift in the overburdened strata, due to previous mining activity and the subsequent unburdening of the rock mass.

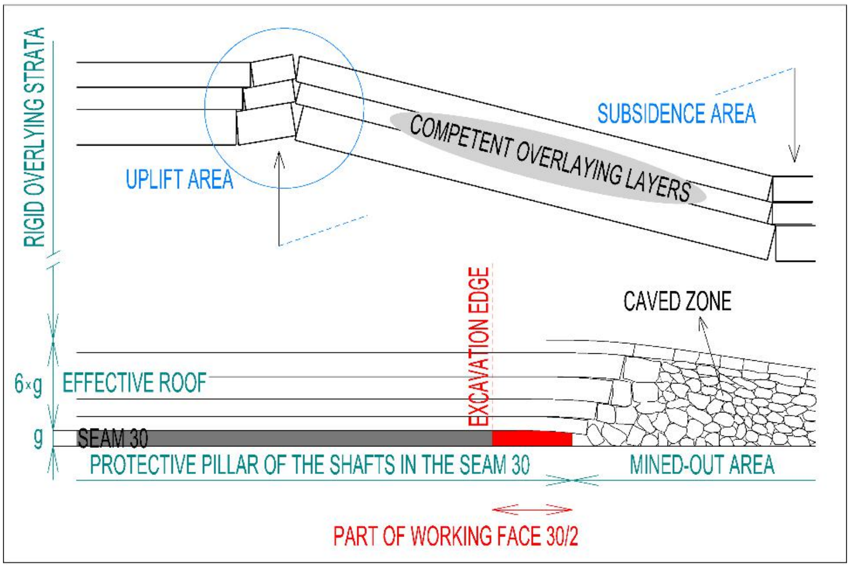

Keywords: ground uplift; subsidence trough; longwall mining; radar interferometry

1. Introduction

Ground surface uplift occurs for various reasons. For example, (Park et al. 2016) describes the thermal-hydrological-mechanical processes within the rock mass surrounding a cavern used for thermal energy storage. Thermal expansion, as a result of the heating of the rock mass from the storage cavern, leads to a ground surface uplift of the order of a few centimetres. The surface uplifts can also occur by CO_2 injection at a CO_2 storage site or pressurised underground rock caverns (Kim et al. 2012). The ground uplift was simulated (Röhmann et al., 2013) and the results show a maximum ground uplift of 0.021 m at the end of CO_2 injection. Another examples describes ground surface uplifts during coal mine flooding. The flooding of the coal mine is carried out by ceasing to pump water out of the mine that was closed. The restoration of hydraulic pressure is long-lasting process, resulting in the reactivation of rock mass movements that can manifest on the ground surface in the form of uplift. Ground surface uplifts were observed in several different coal basins in Europe, for example in Belgium (Devleeschouwer et al., 2008; Vervoort, 2016; Declercq et al., 2017), Poland

(Dudek et al. 2020; Graniczny et al., 2015; M. Dudek et al., 2021), France (Samsonov et al., 2013) and the Netherlands (Caro Cuenca et al., 2013; Bekendam & Pottgens, 1995). These works report on uplift of the ground surface above abandoned coal mines in connection to coal mine flooding. The surface uplift observed by us differ from those works mainly by the fact that the uplift occurred at the site of an actively operating coal mine. The ground surface uplift, due to the influence of underground mining activities during longwall mining, has not been sufficiently described or clarified yet. The main feature of the presented uplift during mining is its temporary occurrence. In terms of the formation of the subsidence trough, the surface uplift can be considered as an anomalous event. In practice, ground surface uplifts occur but, because their values are often no more than twice the mean error (confidence interval) for technical levelling, these uplifts are not usually examined from a geomechanical point of view. This case study provides a description of the ground surface uplift that was observed by precise levelling and satellite radar interferometry (InSAR) (Hu et al. 2016; Ng et al. 2012; Yerro et al. 2014) during longwall mining in the protective pillar of the shaft.

Due to deep mining, displacements and deformations of the ground surface occur (Fathi Salmi et al. 2017; Tichavský et al. 2020). The extent of the effect on the ground surface, during mining operations, is closely related to the mining method used. Longwall mining with controlled caving is the method used for extraction of coal seams. When the seam is extracted by longwall mining, a rectangular mined-out area is formed (Meng et al. 2016; Wang et al. 2017). A subsidence trough forms on the surface, the volume of which corresponds to 85-95% of the volume of the mined deposit. This means that, if the main influence range were extracted and the extracted seam thickness was 3 m, then surface subsidence would reach up to 2.55 m, 2.85 m respectively. The main factors influencing the surface as a result of deep mining are: the mechanical properties of the overlying and surrounding rocks, the thickness of the extracted seam, the geometry of the mined-out area, and the method and the depth of extraction.

However, there are cases when the dynamic formation of the subsidence trough is accompanied by temporary ground surface uplift. It is assumed that surface uplift occurs due to geomechanical changes in the rock mass, accompanied by the displacement and deformation of the overlying strata above the mined-out area. These geomechanical changes have various manifestations (De Santis et al. 2020). A stress field with an enormous concentration of stress can form around the boundaries of the excavation in the overlying strata (Jiránková 2012; Jiránková and Lazecký 2016), but the rock mass can also be stress-relaxed, which occurs when the rigid overlying strata fails (Jiránková, 2010). These phenomena typically occur in cases where there are competent layers in the overlying strata above the mined-out area, i.e. rigid layers which are able to accumulate stress.

The ground surface uplift can be evaluated only from the observed heights of the surface points during the formation of the subsidence trough. From the point of view of predicting subsidence calculations, surface uplift is considered to be unpredictable. The reason for this is that none of the commonly used prediction models allows the calculation of ground surface uplift. All prediction methods work with mining parameters and, to varying degrees, rock mass properties (Ren et al. 1987, 2014; Suchowerska Iwanec et al. 2016; Tajduś 2009) but the results are always values of surface point subsidence. First of all, it is necessary to find the reason why the ground surface uplift occurs in order to be able to suggest a method to predict this phenomenon. The purpose of this paper is to present the measured surface uplift, evaluated from observed surface heights, and to, simultaneously, evaluate the surface using InSAR (Blachowski et al. 2018; Lazecký and Jiránková 2013; Lazecký et al. 2017) to determine the expected cause of the ground surface uplift.

2. Case study area

The CSM Mine is part of the Ostrava–Karvina Coalfield (OKC), which is a deep mining complex in the Czech Republic, situated in the Czech part of the Upper Silesian Coal Basin. The rock mass in the mining area of the CSM-Sever Mine is disturbed by tectonic faults, running in two main directions, namely North-South and West-East. The layers generally dip 9˚ to the North-East. The coal seams in the Carboniferous rock mass occur together with accompanying rocks such as sandstones, siltstones and conglomerates. Above the Carboniferous rock mass is Miocene rock mass which mainly consists of gravel and claystone. The case study evaluates the influence of longwall mining on the surface, with controlled caving in seams 29, 30 and 40. Seams 29 and 30 belong to the Sucha Members and seam 40 belongs to the Saddle Members; both are in the Karvina Formation. The Sucha Members mainly comprise sandstones, siltstones and mudstones. The thickness of the Sucha Members reaches 240 m. On the other hand, the thickness of individual lithological rock types is not large, their value ranges in units of centimetres. The Saddle Members are formed mainly by conglomerates and sandstones and, in the area of the CSM Mine, their thickness ranges in tens of meters. The whole thickness of the Saddle Members is approximately 150 m. The competent layers of sandstones and conglomerates have the ability to accumulate a large amount of stress and contribute to the occurrence of significant geomechanical phenomena (Jiránková et al. 2013).

Table 1. Compression strength values of individual lithological rock types in the OKC (Ptacek et al. 2017)

Rock	Compressive strength range (uniaxial compression) (MPa)	Average value of compressive strength (MPa)
Coal	13.0 – 30.0	21.9
Mudstone	33.0 – 123.0	59.2
Siltstone	21.0 – 219.0	90.3
Fine-grained sandstone	102.0 – 203.0	123.8
Medium-grained sandstone	28.0 – 200.0	73.5
Coarse-grained sandstone	37.0 – 140.0	89.0
Conglomerate	54.0 – 163.0	108.0

Compression strength values of individual lithological rock types in the OKC were obtained by almost 3,000 laboratory tests on intact rock samples (Ptacek et al., 2017) and are shown in Table 1. Laboratory testing of rocks in order to obtain strength parameters usable for FEM numerical calculations, were carried out in the region of the coal mines in the Poland (Tajduś, 2009). Strength parameters and other parameters obtained from laboratory tests of rocks in the Polish part of the Upper Silesian Coal Basin are shown in the Table 2.

Table 2. Parameters of rock mass in the Polish part of the Upper Silesian Coal Basin ((Tajduś, 2009)

Rock mass parameter	Carboniferous rock mass	Miocene rock mass
Density (kg/m^3)	1950 - 2200	2300 - 2500
Cohesion (MPa)	0.03 - 2.20	8.00 – 9.35
Angle of internal friction (°)	15 - 22	37 - 41
Compression strength (MPa)	3.5	22.0 – 40.0
Tensile strength (MPa)	0.63	2.0 – 8.30
Shear strength (GPa)	0.067	0.170 – 0.248
Elastic modulus (GPa)	0.10 – 0.40	0.93 – 1.49
Poisson’s ratio	0.32 – 0.33	0.22 – 0.26

2.1. Mining operations

The case study area shows all mining in the protective pillar Sever, all longwall mining in 2018 and 2019 (the mining period of the evaluated face 30/2) and abandoned, mined-out areas in layer 30 (in the seam of the assessed face 30/2). The full effective area (also known as critical width) is defined as the area in the seam if it is mined-out and the maximum surface subsidence occurs. The radius of the main influence range is determined by the depth of extraction and the angle of main influence. The principle of calculating the radius of the main influence range is explained in the publication (Jiránková 2010). A radius value of 480 m was determined for longwall mining conditions at face 30/2 in seam 30.

In the period May 2014 to October 2017, the room and pillar mining method was operated in the shaft protection pillar Sever at a mining depth ranging from 750 to 900 m. A total of 6503 m of mining works were built and 68 supporting pillars (characteristic of this mining method) were created. The mining works were excavated with an average width of 5.2 m and a height of 3.5 m. The size and shape of the supporting pillars were designed and implemented so that they would be stable in the long-term. The stability of the mining works roof was ensured by means of rock-bolts (Kumar et al. 2019). The mining works were realised in seam 30 and the final realised mining extent used the room and pillar method, as shown in Fig. 1. Subsequently, at the end of 2018, face 29 was mined in the shaft protection pillar Sever. The average extracted seam thickness was 3.00 m and the average mining depth was 700 m.

In the period August 2018 to July 2019, face 30/2 in seam 30 was mined, which significantly encroached on the shaft protection pillar Sever. During the mining of this face, ground surface uplift was registered. The average extracted seam thickness was 2.30 m and the average mining depth was 830 m. The abandoned, mined-out areas in seam 30 (next to the evaluated face 30/2) are shown in Fig. 1. In the main influence range from the evaluated face, seam 30 was mined in the years 2001 to 2004 with an average extracted thickness of 2.10 m. Faces 30/1 (in seam 30), 40/1, 40/2, and 40/3 (in seam 40) were mined in the main influence range of the shaft protection pillar, in 2018 and 2019. The average extracted thickness of face 30/1 was 2.50 m and the average mining depth was 780 m. The average extracted thickness of seam 40 was 5.20 m and the mining depth was in the range of 950 to 1030 m, with respect to the dip of the seam.

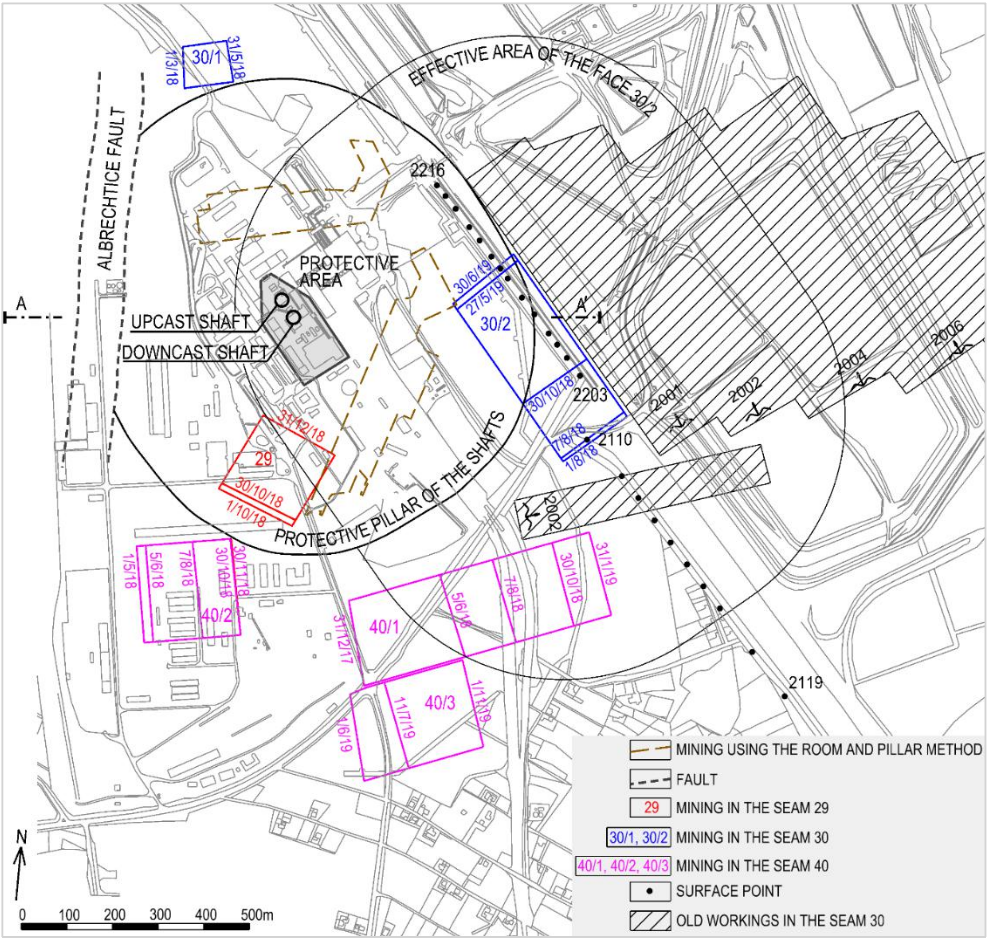

Fig. 1. Illustration of longwall mining in 2018 and 2019, together with observed surface points in lines 2203-2216 and 2110-2119

2.2. Construction the shaft protection pillar Sever

In general, the shaft protection pillars are designed so that safe operation is maintained throughout the mining of the mine, not only in the shafts, but also in the buildings located in the protected area on the surface.

In 1964, conical protective pillars with pillar angles of $\mu_p = 60°$ (for the Miocene rock mass) and $\mu_k = 70°$ (for the Carboniferous Formation) were designed for the downcast and upcast shaft Sever and the protected area on the surface. The downcast and upcast shaft was excavated in a circular cross-section with a diameter of 7.5 m. The reinforcement of the shaft is a combination of brickwork and cast concrete. The intersection of the extracted seam 30 and the downcast shaft (upcast shaft) is at a height of -524.5 m (-525.3 m). The protected surface on the surface is formed by an irregular hexagon, which protects the objects of the buildings of the downcast and upcast shaft, including the engine room and other operational and technical buildings. In the western part, the Albrechtice Fault extends into the defined protective pillar, Fig. 2.

The shaft protection pillar Sever was not designed to be fully protective but used pillar angles which are steeper than the angle of main influence. A fully protective shaft pillar would have the shape of a cone using pillar angles $\mu_p = 55°$ (for the Miocene rock mass) and $\mu_k = 65°$ (for the Carboniferous Formation). Therefore, as a result of mining in the surroundings of the protective pillar, the defined protected area on the surface was also affected.

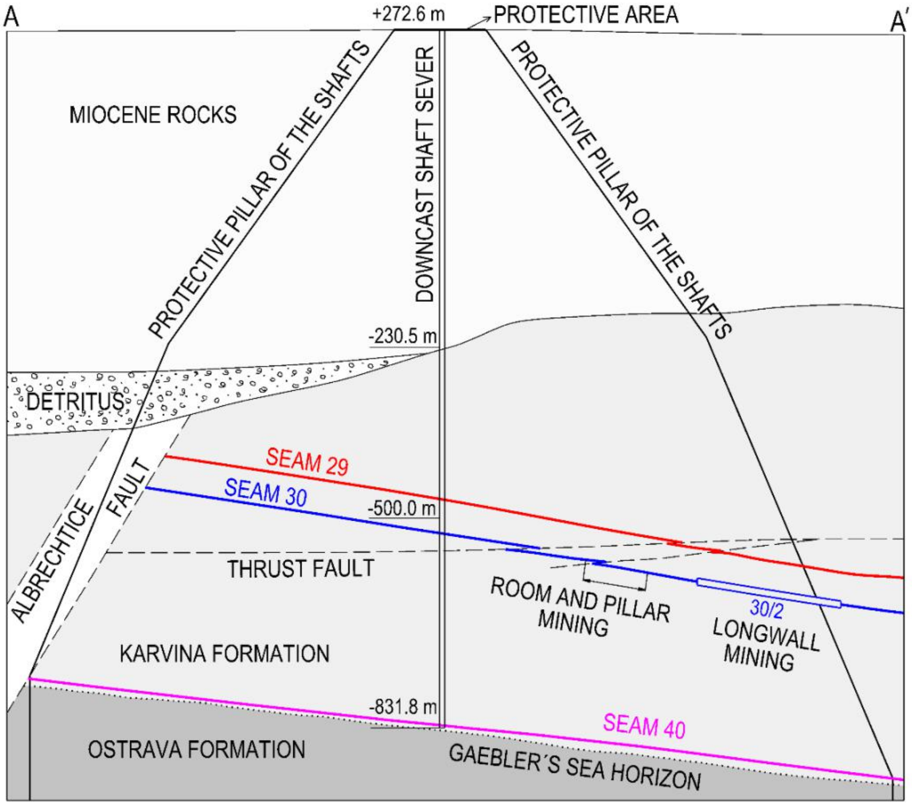

Fig. 2. Cross-section through the shaft protection pillar in the line A-A´

The shafts are designed to resist a certain amount of deformation. This makes it possible to keep the shaft protective pillar smaller than a fully protective design and also to allow limited mining operations in the protective pillar. The impact of mining on the shaft can be minimized by a suitable arrangements of the mining that takes place around (and possibly inside) the protective pillar. A symmetrical mining process, both in terms of space and time, is considered a suitable mining arrangement.

3. The observation of the surface subsidence

In 2018, a surface observation line was designed, whose 16 surface points were stabilised; the first observation was realised before the mining face 30/2 began. The position of surface points 2203-2216 is graphically shown in Fig. 1. The first measurements of the heights of the surface points, including the height connection to the non-influenced area, were taken on 5 June 2018 and 6 June 2018, i.e. approximately two months before the longwall mining of face 30/2. In 2018, two more stages of measurement followed. The second stage was measured at the time of the start of the mining of face 30/2 (August 2018) and the third stage at the end of October 2018. Three stages were then measured in May 2019, July 2019 and November 2019.

The measurement of the heights of the surface points was performed by precise levelling. The connection levelling between point 2203 and point GZ10-64.3, located in the non-influenced area, was 4.8 km long. The verification of the height of point GZ10-64.3 was performed from point GZ 10-64.2, the distance between them being 50 m. The measurements were performed with electronic levelling apparatus: DNA 03 Leica with invar level rod 3 m long. The root mean square errors of the apparatus were 0.3 mm. The measured values were adjusted by the least squares method and the height adjustments of the surface points were determined. The root mean square errors of the height adjustments ranged from 0.5 to 1.1 mm.

The surface subsidence of the points was determined as the difference in the heights of the same point over a period of time, see Fig. 3. The subsidence accuracy depends on the accuracy of the measured point heights of the initial measurement and individual measurements. The mean subsidence error was determined with respect to the principle of the law of accumulation of errors and ranged from 2.1 to 3.5 mm. A value of double this error was used to determine the confidence interval with 5% risk. If the determined subsidence values exceed the confidence interval then they can be considered to be proven with the appropriate risk.

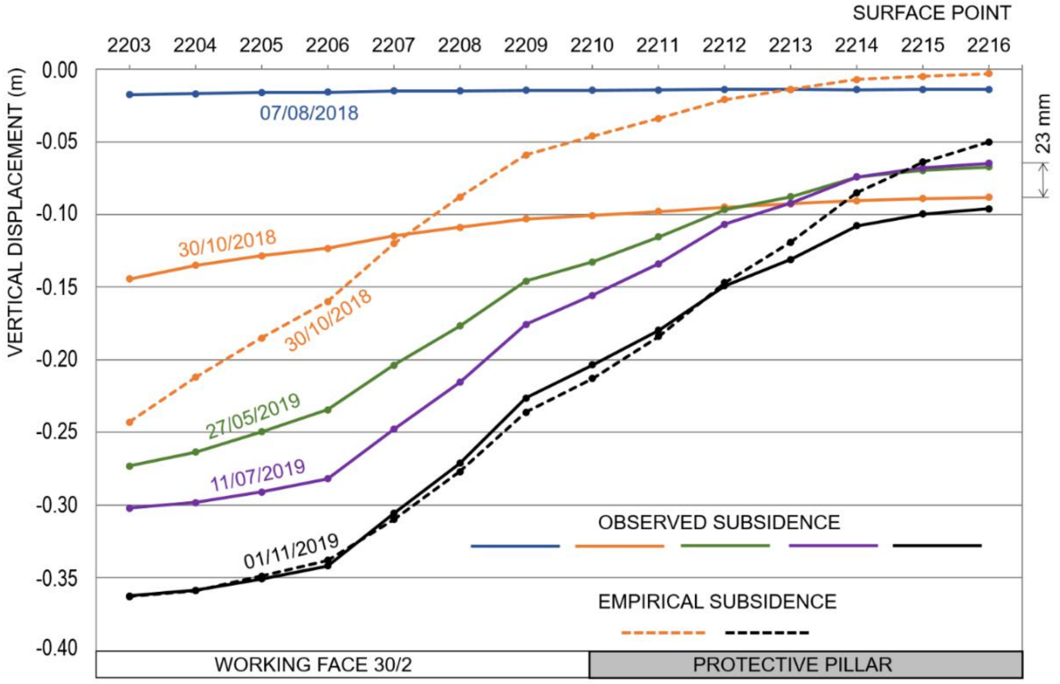

Fig. 3. The surface subsidence in the line of the points 2203-2216, related to the first stage on 6 June 2018.

The subsidence curves (Fig. 3) present the vertical displacements of the surface points in the line 2203-2216 and are referenced to the first measurement stage on 6 June 2018. The largest ground surface uplift (23 mm) was found at point 2216 in the period 30 October 2018 to 11 July 2019. All of the surface points (2213-2216) at which the ground surface uplift were measured were located in the non-mined area.

The height measurement of the surface points in the line 2110-2119 form part of the precise levelling carried out and are situated in the area affected by the previous longwall mining, in the overburden of the evaluated seams. The surface point line is located on the slope of the subsidence trough formed, as can be seen from the results of InSAR data, see below. There was no ground surface uplift in the line 2110-2119 within the levelling period.

4. Empirical surface subsidence

The calculation of empirical subsidence includes longwall mining inside the defined effective area of face 30/2, which was determined by the radius of the main influence range. The empirical subsidence was included in the evaluation to better understand and describe the cause of the ground surface uplift. The empirical subsidence method was established by previous, long-term experience in the local conditions at OKC. In this area, a comparison of measured and empirical subsidence has been carried out over a long period of time, to determine recommendations for the coefficient selection needed for the prediction of surface subsidence.

The empirical calculation depends on an appropriate selection of individual parameters (Jiránková et al. 2020) (Schenk, 1997): the coefficient of extraction (a), the coefficient of efficiency (e) and the time coefficient (φ_t). The empirical value of dynamic surface subsidence (time-dependent subsidence) is given by

(1)

where g is the thickness of mined-out areas and it represents a directly measured variable; its values are given in mining base maps.

The value of the extraction coefficient is chosen according to the mining technology used. Its value expresses the ratio between the volume of the subsidence trough on the surface and the volume of the extracted deposit. For longwall mining with controlled caving, the extraction coefficient is chosen in the range 0.85 to 0.95 (Jiránková, 2010). Based on the experience in OKC, in case of multiple seam mining at depths greater than 700 m, the choice of extraction coefficient does not exceed a value of 0.8. This value assumes that the volume of the subsidence trough formed will occupy 80% of the volume of the extracted deposit and the remaining 20% will remain permanently in the rock mass (with permanent bulking of the caving zone and stratification of the overlaying strata, even in the higher overburden layers).

The efficiency coefficient expresses the dependence of the movement of surface points on the position and extent of the excavation (Zenc 1969). Under OKC conditions, only the Knothe distribution function is used to determine empirical surface subsidence (Knothe, 1984). Its distribution function is based on the similarity between the relationship of the subsidence of surface points on the position and extent of a horizontally-bedded, excavated bearing and the Gauss law of random distribution. The normal distribution can be solved in 3-dimensional space or a 2-dimensional plane. If the mining effects are solved in the 2-dimensional plane, the influence function according to Knothe (Knothe, 1984) is:

(2)

where r is the radius of the main influence range.

The vertical displacements (w_r) of any point located above the excavation boundary are expressed using the distribution function curve:

(3)

where w_{max} is the maximum vertical displacement of the surface point above the excavation. Its value is the product of the extracted thickness and the coefficient of extraction.

The time coefficient (φ_t) is used to calculate the dynamic surface subsidence based on the time function (Schenk, 1997). According to experience in OKC, the time function established by Schenk was used, which has two parameters. The first parameter (T) is time, which is double the time required to mine-out the main influence range and it is assumed that, during this time, 99.6% of the total surface subsidence will be achieved. The second parameter (Re) of the time function is the delay time between the beginning of mining and the first movement on the surface. The time function established by Schenk is given by

(4)

where Δt is the partial time period of empirical subsidence calculation.

To select the parameters of the time function, it was necessary to take into account that the main influence range by longwall mining in 2018 and 2019 was not extracted. Therefore, it was necessary to estimate both parameters from the time development of surface subsidence and experience, with the choice of these parameters similar to OKR conditions. The first parameter was estimated at 55 months (i.e. double the time required to reach the main influence range) and the second at 3 months (i.e. the delay time).

The empirical surface subsidence in the line 2203-2216 was determined for the dates 30 October 2018 and 1 November 2019, see Fig. 3. The empirical subsidence in the line of points 2203-2207 ranged from 99 to 5 mm greater than the observed subsidence on 30 October 2018. The empirical subsidence in the line 2208-2216 ranged from 21 to 85 mm less than the observed subsidence on 30 October 2018. When comparing the empirical and observed subsidence on 1 November 2019, the results were found to be in the line 2203-2212, with a maximum difference of 10 mm at the surface point 2209. However, in the line 2213-2216, observed subsidence from 12 to 46 mm was larger than was calculated, the largest difference occurred at surface point 2216. The results of the comparison between observed and empirical subsidence are clearly shown in Table 3 and the differences are expressed as percentages.

Table 3. Differences between observed and empirical subsidence of surface points in the line 2203 – 2216

Point number	Subsidence to the date on 30/10/2018				Subsidence to the date on 1/11/2019			
	Observed values (m)	Empirical values (m)	Difference between emp. and obs. (m)	Difference to observe ratio (%)	Observed values (m)	Empirical values (m)	Difference between emp. and obs. (m)	Difference to observe ratio (%)
2203	-0.144	-0.243	0.099	68	-0.362	-0.363	0.001	0
2204	-0.135	-0.212	0.077	57	-0.359	-0.359	0.000	0
2205	-0.128	-0.185	0.057	44	-0.351	-0.349	-0.002	-1
2206	-0.123	-0.160	0.037	30	-0.342	-0.338	-0.004	-1
2207	-0.115	-0.120	0.005	5	-0.306	-0.310	0.004	1
2208	-0.109	-0.088	-0.021	-19	-0.271	-0.277	0.006	2
2209	-0.103	-0.059	-0.044	-43	-0.226	-0.236	0.010	4
2210	-0.101	-0.046	-0.055	-54	-0.204	-0.213	0.009	5
2211	-0.098	-0.034	-0.064	-65	-0.180	-0.184	0.004	2
2212	-0.095	-0.021	-0.074	-78	-0.149	-0.147	-0.002	-1
2213	-0.093	-0.014	-0.079	-85	-0.131	-0.119	-0.012	-9
2214	-0.091	-0.007	-0.084	-92	-0.108	-0.085	-0.023	-21
2215	-0.089	-0.005	-0.084	-94	-0.100	-0.064	-0.036	-36
2216	-0.088	-0.003	-0.085	-97	-0.096	-0.050	-0.046	-48

The observed values are determined from the measured height of the surface points and they express the surface subsidence between the stated date (30/10/2018 or 1/11/2019) and the initial measurement that took place (5/6/2018). The empirical values are determined from the empirical calculation of the surface subsidence in the line of points and they express the empirical dynamic subsidence to the stated date (30/10/2018 or 1/11/2019). The mining of the working face 30/2 and all mining that took place during the working face 30/2 mining in the effective area were included in the empirical calculation. The difference between the observed and empirical subsidence is expressed both in terms of its value and the share of the difference in the observed subsidence value. This ratio value represents the significance of the difference due to the observed values.

5. Satellite-borne radar interferometry

There were two reasons for using the ‘Interferometric synthetic aperture radar’ (InSAR) to assess the surface subsidence. The first reason was that this method allows the evaluation of surface subsidence for the whole area of interest (AOI). The second reason was determination of the ground surface vertical displacements by another independent monitoring method.

‘Persistent Scatterers’ (PS) and ‘Small Baseline’ (SB) InSAR techniques, as implemented in ‘Stanford Method for Persistent Scatterers’ (STAMPS) (Hooper 2008), and a derived technique implemented as ‘Looking into Continents from Space: Small Baselines Subset InSAR’ (LiCSBAS) (Morishita et al. 2020), were applied to assess the vertical subsidence of the undermined area using data from the Sentinel-1 ‘Synthetic Aperture Radar’ (SAR) satellite system. The processing approach and methodology are described as the ‘IT4Innovations for Sentinel-1’ (IT4S1) system (Lazecky et al. 2020). In general, the PS method appears to provide more reliable outputs for determining the surface subsidence than the SB method, but it is limited by the character of the observed area, especially distribution of strong radar reflectors that can serve as PS points (e.g. metal structures or buildings) within the scene, to capture vertical changes in time below the observation limits. This limit can be described as a maximal double-difference change of phase of the returned SAR wave, below a quarter of its wavelength (Hanssen 2001). When applied to the Sentinel-1 dataset, assuming stable temporal sampling every 6 days, the STAMPS PS method should be able to reliably assess deformation of up to 8.3 cm/year between neighbouring PS points (connected in the fashion of a Delaunay network), if the data is noise-free. The STAMPS SB approach allows for the processing of points that do not contain strong radar reflectors and are not strongly biased by non-deformation signals in the short term (spreading several temporal samples). The detection limit of 8.3 cm/year between points should be valid in the STAMPS SB case as well, although the SB pixels should be carefully considered, as their signal may be biased by short-term processes (Ansari et al., 2021).

From an application perspective, the major difference in using the LiCSBAS method over the STAMPS SB method is that LiCSBAS requires so-called unwrapped interferograms as its starting point. We have applied an unwrapping procedure of ‘Statistical-Cost, Network-Flow Algorithm for Phase Unwrapping’ (SNAPHU) (Chen and Zebker 2002) to a moderately filtered and down-sampled set of interferograms, without masking noisy pixels. This principle allows the capturing of surface deformations of a higher gradient that would otherwise be limited by the density of the observed points in STAMPS SB, but we may expect a decrease in the reliability of results due to propagated noise.

The AOI is observed from several orbital tracks of Sentinel-1 satellites, from different directions of the satellite line of sight (LOS). All available data from these tracks (Sentinel-1 SAR acquisitions since October 2014 have been temporally sampled about every 12 days; and 6 days since September 2016) were processed by IT4S1 (Lazeckỳ et al. 2020). The LOS measurements of the processing outputs were recalculated to values corresponding to the vertical component of observed deformation in a simplified manner (Lazeckỳ et al., 2020), while assuming no horizontal component. It should be noted that neglecting the horizontal component may cause an additional bias (Wright et al. 2004). A visual inspection of the processed data from relative orbital tracks 51, 175 and 124 confirmed their similarity. Therefore, for the sake of simplicity, only results from relative orbit 124 are presented in this article.

The presented InSAR results were generated from 219 Sentinel-1 data taken between 14 October 2014 and 30 September 2019. The primary output parameter of methods STAMPS PS and STAMPS SB (i.e. the mean deformation velocity) is plotted in Fig. 4, showing an increase of observed points in the case of STAMPS SB. The results are similar but discrepancies in this estimated parameter exist.

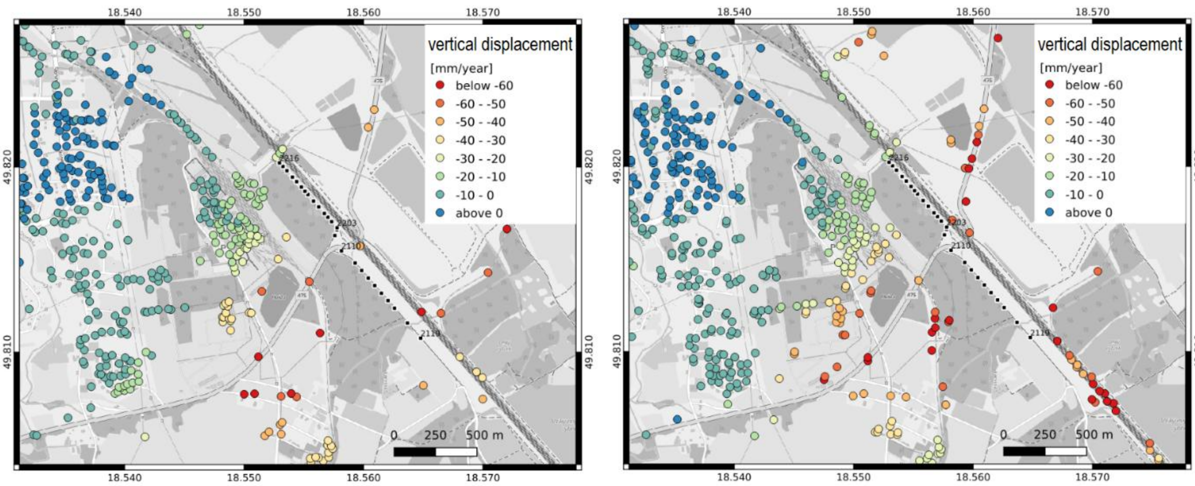

a) STAMPS PS b) STAMPS SB

Fig. 4. Mean velocity of vertical displacements estimated by a) STAMPS PS method and b) STAMPS SB method, both for the Sentinel-1 dataset of relative orbit 124 covering the time period October 2014 to September 2019. Black dots represent levelling points.

In order to compare the InSAR results with the levelling measurements, all InSAR outputs were recomputed by a double-difference towards a reference point nearby the levelling reference point GZ10-64.3. This location is considered stable. However, by using a median of all the points processed by InSAR as an overall (floating) reference, this location may have been subsiding at the rate of approximately 5 mm/year before 2017, as can be identified from Fig. 5. As the vertical displacements vary around zero, the area around the reference points can be considered stable.

As can be observed from Fig. 4, there are only several InSAR points of either PS or SB results close to the levelling points, disallowing preparation of a profile plot similar to the levelling outcomes in Fig. 3. A comparative analysis using one of the levelling points as a local reference has already been performed (Lazeckỳ et al. 2020), showing similarities of outputs between all three applied multi-temporal InSAR methods.

There are only a small number of objects with a stable radar backscatter in the AOI, leading to underestimation of the rate of subsidence, that is considered large for the subsidence troughs of the area. Possible erroneous data points (points of low temporal coherence parameter) were removed from the final STAMPS results. On the other hand, the area is fully covered by the LiCSBAS output using the same dataset (relative orbit 124, covered the period 2016 to 2019). The LiCSBAS mean velocity estimate plotted in Fig. 6 shows that the vertical displacements of the surface above abandoned, mined-out areas were reaching subsidence at the rate of several decimetres per year. It should be noted that LiCSBAS outputs from other relative orbit tracks showed very similar results and, therefore, we present results of only one dataset (orbit 124), without additional efforts on the accurate decomposition to motion vectors or any other merging strategies. The output has been recalculated to a vertical component only. The LiCSBAS time series were clustered into annual periods and the annual rate of displacements were calculated; these are plotted in Fig. 7, together with polygons representing areas of active mining in the corresponding year.

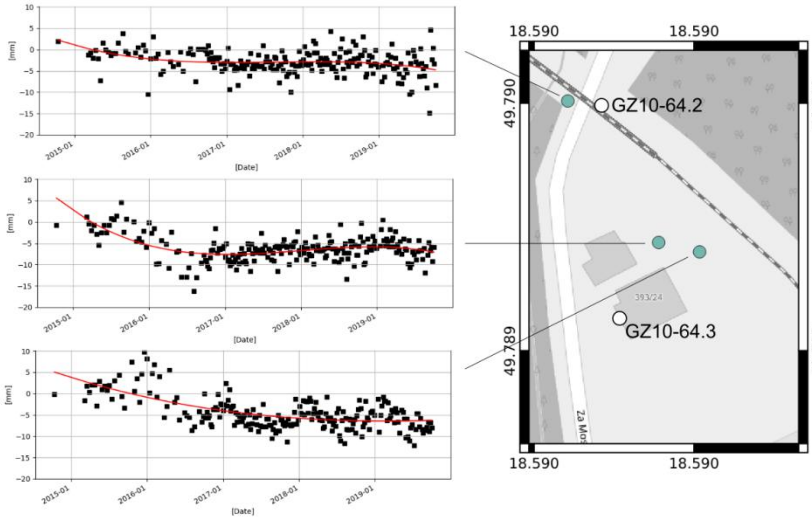

Fig. 5. Time series plots of vertical displacements at PS points near to levelling reference points GZ10-64.2 and GZ10-64.3, referred to a median of all processed PS points in the AOI.

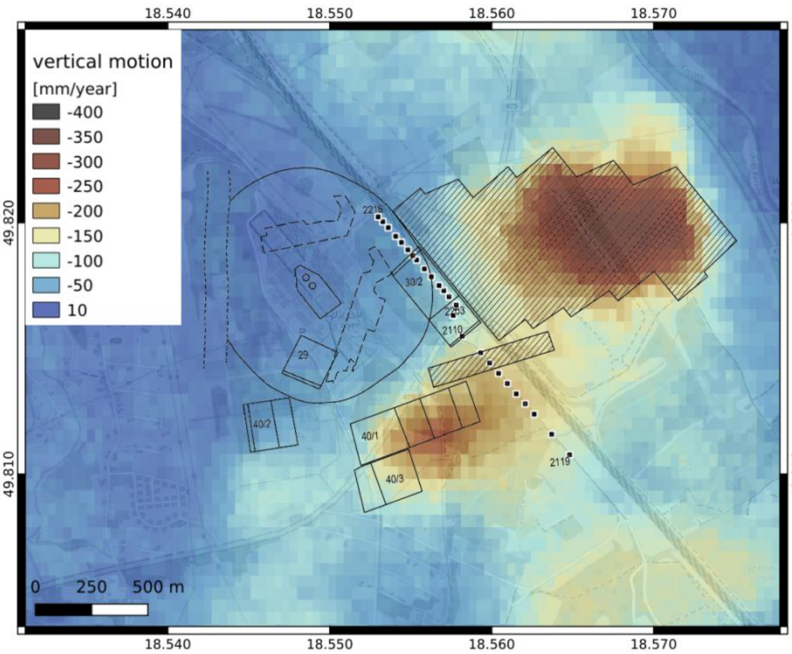

Fig. 6. Mean velocity rate of vertical displacements determined by the LiCSBAS method from the relative orbit 124 dataset and the illustration of mining as shown in Fig. 1, together with longwall mining in 2016 and 2017.

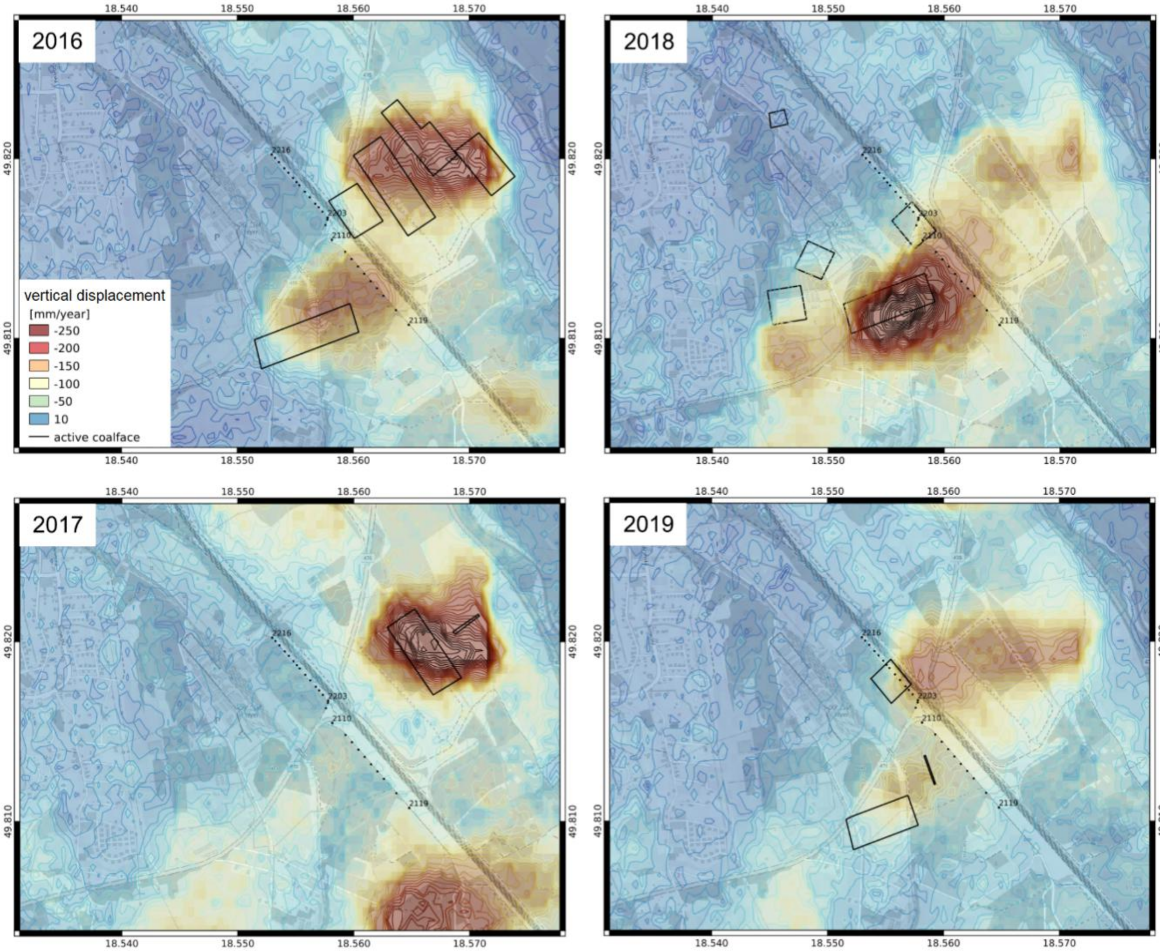

Fig. 7. Vertical displacements determined by the LiCSBAS method (relative orbit 124 dataset) and active mining locations, clustered by individual years.

6. Results and Discussion

The mined area can be divided, from the point of view of the dynamic formation of the subsidence trough, into: areas without the occurrence of ground surface uplift and areas with probable occurrence of temporary ground surface uplift. The ground surface uplifts do not occur if the overlying strata regularly fail during longwall mining (Palchik 2003). Manifestations of the longwall mining at ground surface relate to the failure of rigid overlying strata, which can be complete or incomplete (Jiránková 2012). The cause of surface uplifts is deep inside the rock mass. Therefore only the analysis of mining technical and geological data in connection with the results of surface monitoring (levelling, InSAR) can be used to explain the reason why the ground surface uplift occurs. The following arguments can be considered:

1) Was the rock mass broken by the previous mining at the site where the ground surface uplift occurs and what is the extent and location of the faces?

The longwall mining of face 30/2 was situated in part of the rock mass where the overlying strata was not yet broken (in the shaft protection pillar). Face 30/2 was mined along the western edge of the abandoned mined-out areas, which are located in the same seam. The surface uplifts were observed at a time when almost the entire 30/2 face was extracted. The working face width was 170 m and the advancement length was 140 m at this time. The total mining advancement length of the working face was 186 m. West of the 30/2 face, part of the shaft protection pillar Sever was also mined by the room and pillar method (also in seam 30). Mining by the room and pillar method was completed approximately one year before the beginning of the longwall mining of face 30/2. The location of the mining by the room and pillar method is shown by dashed lines in Fig. 1. Thus, at the time of surface uplifts, the working face of the longwall mining was in the area with the overlaying unbroken strata inside the shaft protection pillar and, at the same time, between the abandoned mined-out areas and those closed to mining by the room and pillar method.

2) What was the influence of undermining on the surface, during longwall mining 30/2, before and after the ground surface uplift occurred?

Before the ground surface uplift occurred, surface subsidence was observed from -144 to -96 mm in the line of points 2203-2216 on 30 October 2018, i.e. at the time as approximately one third of face 30/2 was excavated. The observed subsidence was compared with the empirical subsidence. The empirical subsidence results represent the expected subsidence values with respect to the long-term experiences in the local OKC conditions, i.e. in the area the overlying strata usually failed. The curves of observed subsidence and empirical subsidence shown (from 30 October 2018) intersect and, thus, define the area where the observed subsidence is smaller than expected (2203-2207) and the area where the observed subsidence is greater than expected (2208-2216), see Fig. 3. The observed subsidence in the surface at point 2216 was -88 mm and the empirical subsidence was -3 mm. The compression of the excavation edges and the mining-induced stress in the area resulted in the surface subsidence being 85 mm greater than the expected subsidence for longwall mining on 30 October 2018. When the observed subsidence values are compared for the period between 30 October 2018 and 11 July 2019, the ground surface uplifted in the line of points 2212-2216 and the surface subsidence occurred in the line of points 2203-2212. The largest surface uplift value of 23 mm was observed at point 2216. The following measurement (1 November 2019) shows a good agreement between the observed and empirical subsidence (with the greatest difference of 9 mm being at point 2209) in the line of points 2203-2212. However, at point 2216, the observed subsidence was 46 mm larger than calculated.

3) What vertical displacements occurred on the surface in the abandoned, mined-out area?

The vertical displacements were determined from InSAR by neglecting horizontal component of the line-of-sight velocity output of the LiCSBAS method applied to Sentinel-1 acquisitions taken within the relative satellite orbit 124. Results are shown in Fig. 8 and described in section 5.

The InSAR results from 2018 show the vertical displacement stabilisation after previous mining in the abandoned, mined-out area situated at the eastern edge of the working face 30/2. In general, during the movements' stabilising period, the largest value of vertical displacement occurs in the first year after mining.

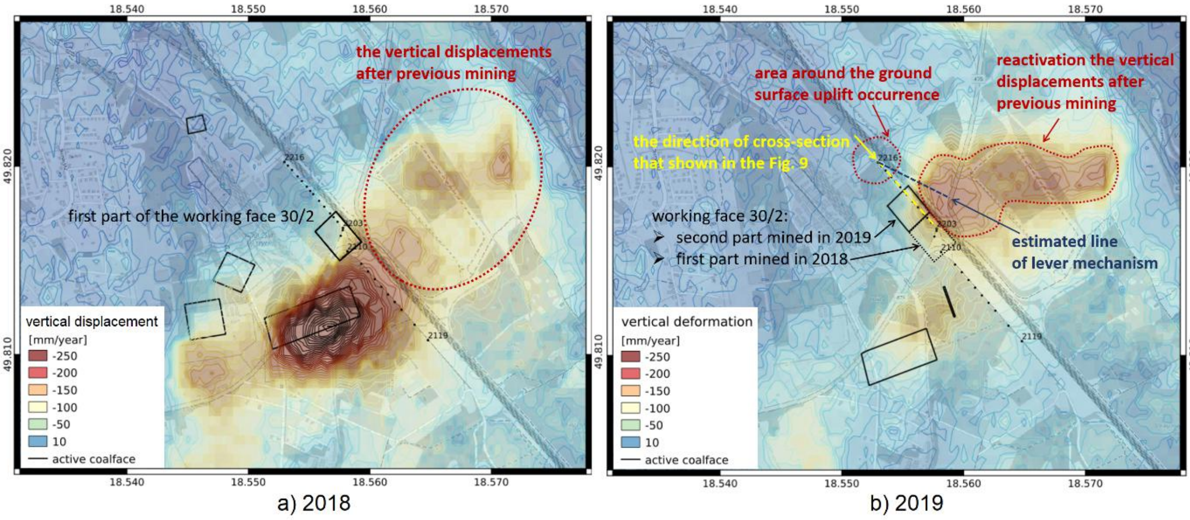

Fig. 8. The vertical displacement interpretation in the abandoned, mined-out area, based on the results from the LiCSBAS method for individual years 2018 and 2019

4) The proposed geomechanical explanation of the ground surface uplift.

The proposed geomechanical explanation is shown in Fig. 9. The mining-induced stress and subsidence preceding the ground surface uplift in the area was smaller than the predicted values. The probable cause of ground surface uplift is deformation in the competent layers (in the uplift area) which has been produced by the subsidence of layers in the abandoned, mined-out area (subsidence area). Through the competent layers that have subsided, to the abandoned, mined-out area, the ground surface uplift was caused when these layers were embedded into the unbroken rock mass. Subsequently, with the development of subsidence in the layers in the abandoned mined-out area, the competent layers above the advancing working face 30/2 were disturbed. This changed the stress fields of the competent layers, causing the previously uplifted area to subside.

Stage 1 shows the competent layers and their mining-induced stress due to previous mining in seam 30. The mining-induced stress in the competent layers was accommodated by surface subsidence that was greater than predicted in the area of the seam 30 protective pillar.

Stage 2 shows the bending competent layers above the edge of the abandoned, mined-out area. This stage is characterised by the competent overlying layers subsiding in the abandoned area, causing a temporary ground surface uplift at the site where these layers were embedded into the previously unbroken rock mass.

In stage 3, the edge of the abandoned, mined-out area was moved due to the advancement of working face 30/2 and this resulted in subsidence of the previously bent, competent layers.

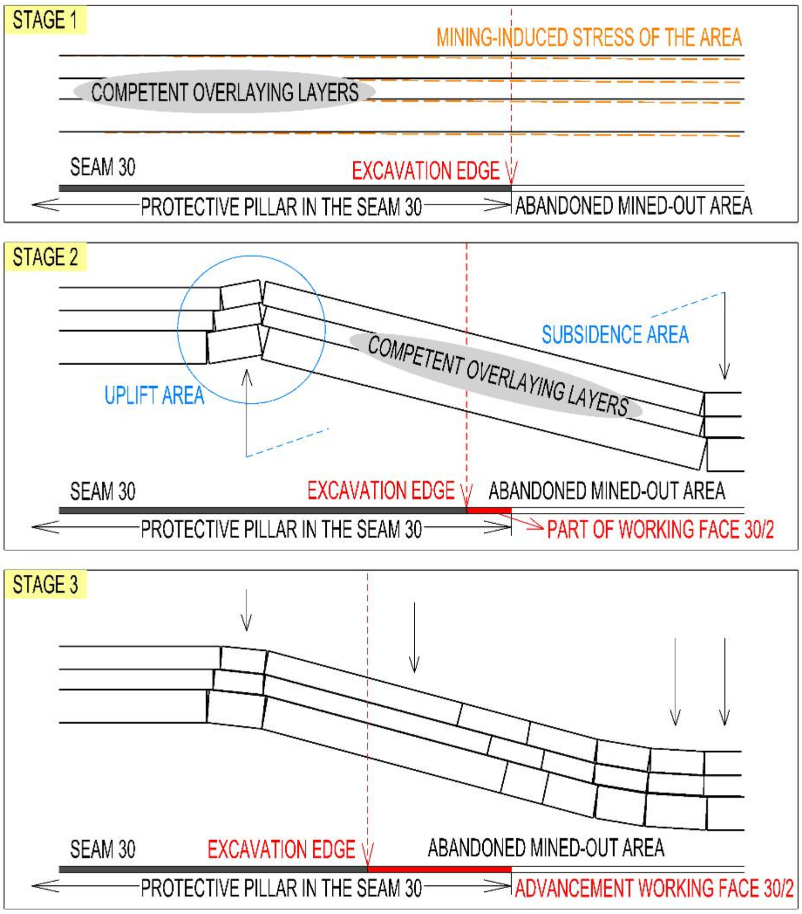

Fig. 9. Illustration of the geomechanical explanation in the direction of the cross-section shown in Fig. 8.

A comparison of observed and empirical subsidence in the surface point line 2003-2216 is given in Sections 3 and 4. There are details the principle of empirical calculation in Section 4. Figure 10 shows the results of this empirical calculation in the effective area of working face 30/2. The calculation of surface subsidence includes all working face in the effective area of the face 30/2, which were mined during the mining of the face 30/2. The different areas of subsidence occurrence determined by the empirical model and InSAR (Fig. 10) show the extent of reactivation of overlaying strata deformations in the abandoned mined-out area, which are the reason of surface uplift occurrence during longwall mining in the area of shafts protective pillar. Note the presented InSAR-based vertical deformation is a result of line-of-sight decomposition (Wright et al., 2004) from cummulative displacements estimated by LiCSBAS from datasets of relative orbits 124 and 175, within the temporal period of the empirical subsidence model, i.e. 08/2018-11/2019 (Fig. 10a).

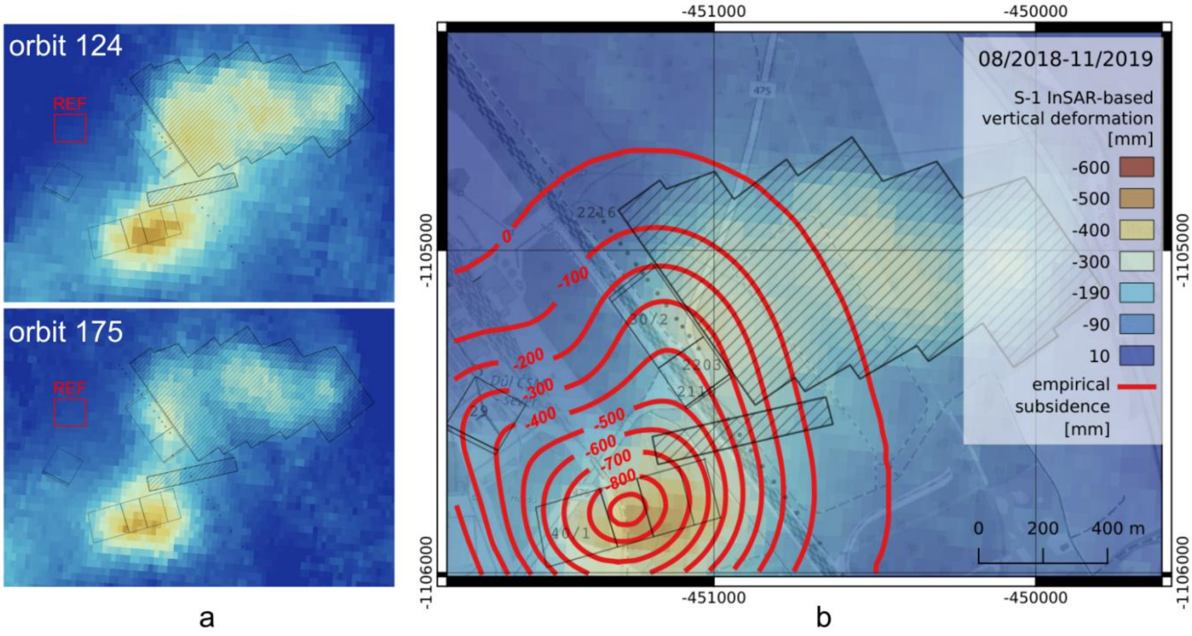

Fig. 10. Vertical surface subsidence between 08/2018-11/2019 from an empirical model and based on Sentinel-1 InSAR: a) output from separate datasets (relative orbits 124 and 175) with same colour scale as b; b) empirical subsidence contours over averaged vertical InSAR displacements from both orbits. InSAR spatial reference area is plotted as 'REF' box.

The mechanism of the reason of uplift of the ground surface was further analysed with theoretical simulation. It appears that it will be worthwhile to estimate uplift by theoretical simulation based on "See-Saw" mechanism which interprets part of competent rock as a beam that can be considered as lever, i.e. one side of lever arm moves down and opposite side of lever arm moves up and just this arm effects on the overlying rock mass and induced the local uplift, Fig. 8. One side of lever arm was estimated on basis of distance between the mined-out area edge and reactivated area. Opposite side of lever arm was estimated on basis of distance between the mined-out area edge and area of surface uplift. The average mining depth in seam 30 was 830 m. If we consider that the fractured zone of the excavation in seam 30 is 13.8 m (i.e. six times the mined seam thickness (Jiránková et al., 2020)), then the lever mechanism can be estimated at a depth of 816 m. The estimated line of lever mechanism with length of 485 m is shown in Fig. 8. However, the location of the joint between opposite side of lever arms cannot be clearly determined. In addition to breaking the overlying layers, we must also take into account the layers press down direction to the excavation. The estimated length of the lever mechanism line (485 m) correspond to the arm length of 435 m that moves down and the arm length of 50 m that moves up. The values explain the uplift (23 mm) on the one side of lever arm and the subsidence (200 mm) on the opposite side of lever arm.

Another useful analysis of the reason of ground surface uplift could be a numerical simulation. In the area of the Karvina sub-basin, the rock mass is composed of Carboniferous and Miocene rocks which are different physical-mechanical properties. While the behaviour of Carboniferous rocks is elastic, the behaviour of Miocene rocks is plastic/elastic. Therefore, the reason of surface uplifts formation is located in Carboniferous rocks, i.e. in an elastic rock environment. The deformation of the Carboniferous rocks further spreads through the Miocene rocks until they reach the surface. A useful numerical simulation must include both the shaft protection area and the abandoned mined-out area, i.e. the area of occurrence of surface reactivation. However, strength parameters and other parameters obtained from laboratory tests on intact rock samples cannot be used for numerical simulation to reactivate the deformations of rock mass disturbed by previously mining in abandoned mined-out area. At present, only this surface uplift occurrence was described. As soon as further example studies of the surface uplift occurrences around of the shafts protective pillars are described, it will be possible to propose an estimation of the mechanical parameters of the rock mass in the reactivated area and numerically model the cause of the surface uplifts.

7. Conclusions

Clarification of the occurrence of ground surface uplift is of the most importance, mainly because none of the methods for predicting surface subsidence allow the calculation of the surface uplift. The expected occurrence of the uplift can only be predicted on the basis of experience, from areas in which the uplift has already occurred.

In this paper, the observed ground surface uplift during longwall mining, carried out lengthwise with abandoned mined-out areas in the same seam, was described. The following conclusions can be drawn from the work.

1) Ground surface uplift occurred during the working of the first face in the area of the intact strata due to previous mining. Through the overlying competent layers, the subsidence of the overburden in the area of previous mining was manifested by ground surface uplift at the site where these layers were embedded into the previously unbroken rock mass.

2) When the surface uplifts occurred, the continuous advancement length of the working face in the area of the intact strata was 410 m, with an excavated width of 170 m.

3) The comparison of the observed subsidence with empirical vertical displacements displays differences from -0.079 to -0.085 m, i.e. the observed subsidence is 85 to 97% greater than were predicted for the part of the line between points 2213 and 2216. Thus, it was found that the surface uplifts were preceded by mining-induced stress of the area.

4) The three stages of competent layer deformation advancement are based on the proposed geomechanical explanation. Stage 1 is the mining-induced stress of the competent layers, stage 2 is the bending of the layers above the edge of the abandoned area and stage 3 is the subsidence of the competent layers due to disturbance by the advancement of the working face 30/2.

The described occurrence of ground surface uplift during subsidence trough formation can be expected in places where longwall mining expands into the areas where the overlying strata are still unbroken, such as a shaft protection pillar or areas where the seams have not yet been extracted.

Declaration of Competing Interest

The authors declare that they have no known competing financial interests or personal relationships that could have appeared to influence the work reported in this paper.

Acknowledgements

This article was written in connection with project No. 899192 PostMinQuake RFCS-2019. The presented work was also supported by a project for the long-term conceptual development of research organisations (identification code: RVO: 68145535), and by The Ministry of Education, Youth and Sports from the National Programme of Sustainability (NPU II) projects ‘IT4Innovations excellence in science - LQ1602’ and ‘e-INFRA CZ – LM2018140’.

References

Ansari, H., Zan, F. D., Parizzi, A. "Study of Systematic Bias in Measuring Surface Deformation With SAR Interferometry," *IEEE Transactions on Geoscience and Remote Sensing*, *59 (2)*, pp. 1285-1301, 2021

Bekendam, R. F., & Pottgens, J. J. (1995). Ground movements over the coal mines of southern Limburg, the Netherlands, and their relation to rising mine waters. *Land Subsidence. Proc. International Symposium,* *The Hague, 1995*. https://doi.org/10.1016/s0148-9062(97)87575-4

Blachowski, J., Jiránková, E., Lazecký, M., Kadlečík, P., & Milczarek, W. (2018). Application of satellite radar interferometry (PSInSAR) in analysis of secondary surface deformations in mining areas. Case studies from Czech Republic and Poland. *Acta Geodynamica et Geomaterialia*, *15*(2). https://doi.org/10.13168/AGG.2018.0013

Caro Cuenca, M., Hooper, A. J., & Hanssen, R. F. (2013). Surface deformation induced by water influx in the abandoned coal mines in Limburg, The Netherlands observed by satellite radar interferometry. *Journal of Applied Geophysics*, *88*. https://doi.org/10.1016/j.jappgeo.2012.10.003

Chen, C. W., & Zebker, H. A. (2002). Phase unwrapping for large SAR interferograms: Statistical segmentation and generalized network models. *IEEE Transactions on Geoscience and Remote Sensing*, *40*(8). https://doi.org/10.1109/TGRS.2002.802453

De Santis, F., Renaud, V., Gunzburger, Y., Kinscher, J., Bernard, P., & Contrucci, I. (2020). In situ monitoring and 3D geomechanical numerical modelling to evaluate seismic and aseismic rock deformation in response to deep mining. *International Journal of Rock Mechanics and Mining Sciences*, *129*. https://doi.org/10.1016/j.ijrmms.2020.104273

Declercq, P. Y., Gerard, P., Pirard, E., Perissin, D., Walstra, J., & Devleeschouwer, X. (2017). Subsidence related to groundwater pumping for breweries in Merchtem area (Belgium), highlighted by Persistent Scaterrer Interferometry. *International Journal of Applied Earth Observation and Geoinformation*, *63*. https://doi.org/10.1016/j.jag.2017.07.012

Devleeschouwer, X., Declercq, P.-Y., Flamion, B., Brixko, J., Timmermans, A., & Vanneste, J. (2008). Uplift revealed by radar interferometry around Liège (Belgium): a relation with rising mining groundwater. *Proceedings of the Post-Mining Symposium*.

Dudek, M., Rusek, J., Tajduś, K., & Słowik, L. (2021). Analysis of steel industrial portal frame building subjected to loads resulting from land surface uplift following the closure of underground mines. *Archives of Civil Engineering*, *67*(3).

Dudek, Mateusz, Tajduś, K., Misa, R., & Sroka, A. (2020). Predicting of land surface uplift caused by the flooding of underground coal mines – A case study. *International Journal of Rock Mechanics and Mining Sciences*, *132*. https://doi.org/10.1016/j.ijrmms.2020.104377

Fathi Salmi, E., Nazem, M., & Karakus, M. (2017). Numerical analysis of a large landslide induced by coal mining subsidence. *Engineering Geology*, *217*. https://doi.org/10.1016/j.enggeo.2016.12.021

Graniczny, M., Colombo, D., Kowalski, Z., Przyłucka, M., & Zdanowski, A. (2015). New results on ground deformation in the Upper Silesian Coal Basin (southern Poland) obtained during the DORIS Project (EU-FP 7). *Pure and Applied Geophysics*, *172*(11). https://doi.org/10.1007/s00024-014-0908-6

Hanssen, R. F. (2001). Radar Interferometry: Data Interpretation and Error Analysis (Remote Sensing and Digital Image Processing). In *Springer*.

Hooper, A. J. (2008). A multi-temporal InSAR method incorporating both persistent scatterer and small baseline approaches. *Geophysical Research Letters*, *35*(16). https://doi.org/10.1029/2008GL034654

Hu, J., Ding, X. L., Li, Z. W., Zhang, L., Zhu, J. J., Sun, Q., & Gao, G. J. (2016). Vertical and horizontal displacements of Los Angeles from InSAR and GPS time series analysis: Resolving tectonic and anthropogenic motions. *Journal of Geodynamics*, *99*. https://doi.org/10.1016/j.jog.2016.05.003

Jiránková, E. (2010). Assessment of rigid overlying strata failure in face mining. *Central European Journal of Geosciences*, *2*(4). https://doi.org/10.2478/v10085-010-0014-7

Jiránková, E. (2012). Utilisation of surface subsidence measurements in assessing failures of rigid strata overlying extracted coal seams. *International Journal of Rock Mechanics and Mining Sciences*, *53*, 111–119. https://doi.org/10.1016/j.ijrmms.2012.05.007

Jiránková, E., & Lazecký, M. (2016). Specifics in the formation of subsidence troughs in the Karvina part of the Ostrava-Karvina coalfield with the use of radar interferometry. *Acta Geodynamica et Geomaterialia*, *13*(3). https://doi.org/10.13168/AGG.2016.0008

Jiránková, E., Staš, L., Kajzar, V., & Doležalová, H. (2013). Mechanism of rigid overlaying of Carboniferous strata failure in face mining in the case of a multiseams deposit. *Acta Geodynamica et Geomaterialia*, *10*(2). https://doi.org/10.13168/AGG.2013.0019

Jiránková, E., Waclawik, P., & Nemcik, J. (2020). Assessment of models to predict surface subsidence in the Czech part of the upper silesian coal basin-case study. *Acta Geodynamica et Geomaterialia*, *17*(4). https://doi.org/10.13168/AGG.2020.0034

Kim, H. M., Park, D., Ryu, D. W., & Song, W. K. (2012). Parametric sensitivity analysis of ground uplift above pressurized underground rock caverns. *Engineering Geology*, *135–136*. https://doi.org/10.1016/j.enggeo.2012.03.006

Knothe, S. (1984). *Prediction of the mining influence*. https://scholar.google.com/scholar?cluster=1587786234568473542&hl=cs&as_sdt=2005&sciodt=0,5

Kumar, A., Waclawik, P., Singh, R., Ram, S., & Korbel, J. (2019). Performance of a coal pillar at deeper cover: Field and simulation studies. *International Journal of Rock Mechanics and Mining Sciences*, *113*. https://doi.org/10.1016/j.ijrmms.2018.10.006

Lazeckỳ, M., Hatton, E., González, P. J., Hlaváčová, I., Jiránková, E., Dvořák, F., Šustr, Z., & Martinovič, J. (2020). Displacements monitoring over Czechia by IT4S1 system for automatised interferometric measurements using Sentinel-1 data. *Remote Sensing*, *12*(18). https://doi.org/10.3390/RS12182960

Lazecký, M., & Jiránková, E. (2013). Optimization of satellite InSAR techniques for monitoring of subsidence in the surroundings of Karviná Mine: Lazy plant. *Acta Geodynamica et Geomaterialia*, *10*(1).

Lazecký, M., Jiránková, E., & Kadlečík, P. (2017). Multitemporal monitoring of Karvina subsidence troughs using sentinel-1 and TERRASAR-X interferometry. *Acta Geodynamica et Geomaterialia*, *14*(1). https://doi.org/10.13168/AGG.2016.0027

Meng, Z., Shi, X., & Li, G. (2016). Deformation, failure and permeability of coal-bearing strata during longwall mining. *Engineering Geology*, *208*. https://doi.org/10.1016/j.enggeo.2016.04.029

Morishita, Y., Lazecky, M., Wright, T. J., Weiss, J. R., Elliott, J. R., & Hooper, A. (2020). LiCSBAS: An open-source insar time series analysis package integrated with the LiCSAR automated sentinel-1 InSAR processor. *Remote Sensing*, *12*(3). https://doi.org/10.3390/rs12030424

Ng, A. H. M., Ge, L., Zhang, K., & Li, X. (2012). Estimating horizontal and vertical movements due to underground mining using ALOS PALSAR. *Engineering Geology*, *143–144*. https://doi.org/10.1016/j.enggeo.2012.06.003

Palchik, V. (2003). Formation of fractured zones in overburden due to longwall mining. *Environmental Geology*, *44*(1). https://doi.org/10.1007/s00254-002-0732-7

Park, J. W., Rutqvist, J., Ryu, D., Park, E. S., & Synn, J. H. (2016). Coupled thermal-hydrological-mechanical behavior of rock mass surrounding a high-temperature thermal energy storage cavern at shallow depth. *International Journal of Rock Mechanics and Mining Sciences*, *83*. https://doi.org/10.1016/j.ijrmms.2016.01.007

Ptacek, J., Konicek, P., Holecko, J., Przeczek, A., Waclawik, P., Pavelek, Z., Macura, M., Kajzar, V., & Kukutsch, R. (2017). *Rockbursts in Ostrava-Karvina Coalfield*. Institute of Geonics of the Czech Academy of Sciences.

Ren, G., Li, G., & Kulessa, M. (2014). Application of a Generalised Influence Function Method for Subsidence Prediction in Multi-seam Longwall Extraction. *Geotechnical and Geological Engineering*, *32*(4). https://doi.org/10.1007/s10706-014-9787-y

Ren, G., Reddish, D. J., & Whittaker, B. N. (1987). Mining subsidence and displacement prediction using influence function methods. *Mining Science and Technology*, *5*(1). https://doi.org/10.1016/S0167-9031(87)90966-2

Röhmann, L., Tillner, E., Magri, F., Kühn, M., & Kempka, T. (2013). Fault reactivation and ground surface uplift assessment at a prospective German CO2 storage site. *Energy Procedia*, *40*. https://doi.org/10.1016/j.egypro.2013.08.050

Samsonov, S., d'Oreye, N., & Smets, B. (2013). Ground deformation associated with post-mining activity at the French-German border revealed by novel InSAR time series method. *International Journal of Applied*

Earth Observation and Geoinformation, *23*(1). https://doi.org/10.1016/j.jag.2012.12.008

Schenk, J. (1997). *Time factor: an important element in the study of the subsidence trough dynamics*. VSB - Technical University of Ostrava.

Suchowerska Iwanec, A. M., Carter, J. P., & Hambleton, J. P. (2016). Geomechanics of subsidence above single and multi-seam coal mining. *Journal of Rock Mechanics and Geotechnical Engineering*, *8*(3). https://doi.org/10.1016/j.jrmge.2015.11.007

Tajduś, K. (2009). New method for determining the elastic parameters of rock mass layers in the region of underground mining influence. *International Journal of Rock Mechanics and Mining Sciences*, *46*(8). https://doi.org/10.1016/j.ijrmms.2009.04.006

Tichavský, R., Jiránková, E., & Fabiánová, A. (2020). Dating of mining-induced subsidence based on a combination of dendrogeomorphic methods and in situ monitoring. *Engineering Geology*, *272*. https://doi.org/10.1016/j.enggeo.2020.105650

Vervoort, A. (2016). Surface movement above an underground coal longwall mine after closure. *Natural Hazards and Earth System Sciences*, *16*(9). https://doi.org/10.5194/nhess-16-2107-2016

Wang, S., Li, X., & Wang, S. (2017). Separation and fracturing in overlying strata disturbed by longwall mining in a mineral deposit seam. *Engineering Geology*, *226*. https://doi.org/10.1016/j.enggeo.2017.06.015

Wright, T. J., Parsons, B. E., & Lu, Z. (2004). Toward mapping surface deformation in three dimensions using InSAR. *Geophysical Research Letters*, *31*(1). https://doi.org/10.1029/2003GL018827

Yerro, A., Corominas, J., Monells, D., & Mallorquí, J. J. (2014). Analysis of the evolution of ground movements in a low densely urban area by means of DInSAR technique. *Engineering Geology*, *170*, 52–65. https://doi.org/10.1016/j.enggeo.2013.12.002

Zenc, M. (1969). Comparison of Bals's and Knothe's methods of calculating surface movements due to underground mining. *International Journal of Rock Mechanics and Mining Sciences And*, *6*(2). https://doi.org/10.1016/0148-9062(69)90033-3